NeuroImage 260 (2022) 119422

Contents lists available at ScienceDirect

NeuroImage

journal homepage: www.elsevier.com/locate/neuroimage

Estimating the influence of stroke lesions on MEG source reconstruction

Maria Carla Piastra [a,b,c,*], Robert Oostenveld [b,d], Jan Mathijs Schoffelen [b], Vitória Piai [b,e]

[a] Radboud University Medical Center, Donders Institute for Brain, Cognition and Behaviour, Department of Cognitive Neuroscience, Nijmegen, The Netherlands
[b] Radboud University, Donders Institute for Brain, Cognition and Behaviour, Nijmegen, The Netherlands
[c] Clinical Neurophysiology, Technical Medical Centre, Faculty of Science and Technology, University of Twente, Enschede, The Netherlands
[d] NatMEG, Karolinska Institutet, Stockholm, Sweden
[e] Radboud University Medical Center, Donders Institute for Brain, Cognition and Behaviour, Department of Medical Psychology, Nijmegen, The Netherlands

ARTICLE INFO

Keywords:
MEG
Source localization
Chronic stroke
Brain asymmetries
Volume conduction modeling
FEM

ABSTRACT

Source reconstruction of magnetoencephalography (MEG) has been used to assess brain reorganization after brain damage, such as stroke. Lesions result in parts of the brain having an electrical conductivity that differs from the normal values. The effect this has on the forward solutions (i.e., the propagation of electric currents and magnetic fields generated by cortical activity) is well predictable. However, their influence on source localization results is not well characterized and understood. This is specifically a concern for patient studies with asymmetric (i.e., within one hemisphere) lesions focusing on asymmetric and lateralized brain activity, such as language. In particular, it is good practice to consider the level of geometrical detail that is necessary to compute and interpret reliable source reconstruction results.

To understand the effect of lesions on source estimates and propose recommendations to researchers working with clinical data, in this study we consider the trade off between improved accuracy and the additional effort to compute more realistic head models, with the aim to answer the question whether the additional effort is worth it. We simulated and analyzed the effects of a stroke lesion (i.e., an asymmetrically distributed CSF-filled cavity) in the head model with three different sizes and locations when performing MEG source reconstruction using a finite element method (FEM). We compared the effect of the lesion with a homogeneous head model that neglects the lesion. We computed displacement and attenuation/amplification maps to quantify the localization errors and signal magnitude modulation.

We conclude that brain lesions leading to asymmetrically distributed CSF-filled cavities should be modeled when performing MEG source reconstruction, especially when investigating deep sources or post-stroke hemispheric lateralization of functions. The strongest effects are not only visible in perilesional areas, but can extend up to 20 mm from the lesion. Bigger lesions lead to stronger effects impacting larger areas, independently from the lesion location. Lastly, we conclude that more priority should be given to usability and accessibility of the required computational tools, to allow researchers with less technical expertise to use the improved methods that are available but currently not widely adopted yet.

1. Introduction

Magnetoencephalography (MEG) is a non-invasive neuroimaging technique that combines a high spatial and temporal resolution. Initially used clinically mainly to identify epileptic foci (e.g., Duncan et al. (2016)), MEG has advantages for superficial tangential cortical activity over electroencephalography (EEG) because of its higher spatial resolution and lower sensitivity to noise and cerebrospinal-fluid (CSF) channeling effects (Piastra et al., 2021b; Vorwerk et al., 2014). Using sophisticated source reconstruction techniques, whole-head multichannel MEG sensors allow for source reconstruction with a good spatial resolution, boosting the clinical use of MEG technology to analyze more complex problems of predicting recovery and assessing brain reorganization after brain damage, such as stroke.

Globally, stroke is one of the most common causes of death and adult disability (disability-adjusted life-years). The World Stroke Organization estimates that one in four adults over the age of 25 will have a stroke in their lifetime. Apart from physical disability, stroke survivors are prone to develop cognitive impairment, with a prevalence of more than 20% in the subacute and chronic phases (e.g., Douiri et al. (2013)). Some of the cognitive domains known to be affected by stroke, including

* Corresponding author.
E-mail address: mariacarla.piastra@radboudumc.nl (M.C. Piastra).

https://doi.org/10.1016/j.neuroimage.2022.119422.
Received 30 August 2021; Received in revised form 20 May 2022; Accepted 18 June 2022
Available online 30 June 2022.

language, memory, executive function, and visuospatial function (e.g., Hurford et al. (2013)), are associated with lateralized brain activity. The aforementioned advantages of MEG make it an important tool to study functional changes in the brain following stroke. However, since naturally occurring lesions are asymmetrical (i.e., within one hemisphere) in the large majority of cases, a within-patient left/right hemispheric comparison may become flawed if the observation of the function (brain activity) in the left and right hemispheres is different due to a trivial difference in volume conduction that has no bearing on brain function.

MEG source reconstruction, or estimating the position and/or strength of the neural sources of the MEG data that is recorded over the scalp, requires solving the so-called 'inverse problem', which is ill-posed with no unique solution (Brette and Destexhe, 2012). Solving the inverse problem requires model assumptions on the sources. The subsequent accuracy of the inverse solution depends, among other factors, on the accuracy of the so-called 'forward solution'. The forward solution or forward model comprises the spatial distribution of the MEG signals due to the activity of known sources. The forward solution requires a volume conduction model of the head (or 'head model') in order to model the distribution of neuronal and volume currents. It is custom to use simplified approximations of the head geometry, as these allow for computationally efficient and (quasi-) analytical (Nolte, 2003; Sarvas, 1987) solutions, which are accurate enough in most applications. For more complex geometries, the solution needs to be computed numerically (Mosher et al., 1999). Both the construction of more complex geometries and the numeric computation of the forward model add a level of complexity to the analysis pipeline and work to be done by the researcher, which is not always explicitly considered when considering the benefits of potentially improved forward model accuracy.

There are nevertheless particular scenarios for which a higher complexity and resolution of the head model is justified, for example when the researcher's focus is on deep sources, such as medial temporal lobe structures. The case that we consider here comprises lesions that form localized and asymmetric 'pockets' in the brain with a conductivity that is substantially different from the neighboring areas, such as chronic stroke lesions resulting in cavities filled with cerebrospinal fluid (CSF).

1.1. Rationale of the present study

The goal of the present paper is to model the effect of asymmetrically distributed CSF-filled cavities, which we do through the use of stroke-induced lesions, on MEG source reconstruction to study the effects of asymmetrical anatomical abnormalities in asymmetric brain activity, such as language lateralization. There is a vast literature on the effects of modeling head compartments with different conductivity in the forward (Haueisen et al., 1997; Stenroos et al., 2014; Vorwerk et al., 2014; Wolters et al., 2006) and inverse (Bénar and Gotman, 2002; Dannhauer et al., 2011; Oostenveld and Oostendorp, 2002) solutions, and, in a reciprocal sense (Wagner et al., 2016), in brain stimulation simulations (Datta et al., 2011; Minjoli et al., 2017; Schmidt et al., 2015; Wagner et al., 2013)). Nevertheless, while CSF shunting effects on volume currents and thereby on forward (and inverse) solutions are well known (see, e.g., Vorwerk et al. (2014)), these effects have not been well quantified in the particular scenario of stroke lesions or, more generally, asymmetric localized cavities. It is good practice to consider the level of geometrical detail that is necessary to compute and interpret reliable source reconstruction results. To propose concrete recommendations, we study whether the additional effort required for more realistic head models is worth it, using analysis pipelines based on readily available FEM solvers and easy-to-use toolboxes.

To focus on the asymmetries due to CSF-filled cavities and their effects on source reconstruction, we want to ignore the normally occurring asymmetries between the left and right hemispheres. Therefore, we artificially symmetrized an MRI scan along the midline before building the head model. Thus, the normal asymmetries such as differences in cortical volume and folding between the hemispheres are excluded from our model. The model is nevertheless based on a real anatomical MRI and the asymmetry along the anterior-posterior direction is retained in the model.

Taking the head model with the lesion to represent the 'ground truth' and using it as the forward model to simulate the measured MEG data, we performed source reconstruction assuming a head model with no lesion. This represents a scenario in which a researcher records data from a patient with a stroke lesion and does not include the lesion in the analysis of that data. We investigate the effects of neglecting this abnormal asymmetry and quantify the displacement of estimated source locations and the attenuation/amplification of the amplitude of the reconstructed source activity.

The shape, size, location, and composition of lesions vary from subject to subject. Since individual lesions can be irregular in shape, accounting for them in the head model is challenging if the forward solver requires specific constraints (e.g. smoothness or regularity) of the geometric model of the head. For example, in most Boundary Element Method (BEM) implementations, the head model needs to be represented as a set of nested non-intersecting surfaces (Kybic et al., 2006), which are not straightforward to create from anatomical MRIs with lesions. Moreover, more surfaces and more detail in these surfaces implies more degrees of freedom in the linear system to be solved, resulting in an increase of the computational effort. There are nevertheless state-of-the-art BEM solutions for arbitrary piecewise homogeneous conductors (Stenroos, 2016). In the case of other numerical methods, such as the finite volume methods (Cook and Koles, 2006), the finite difference methods (e.g., Montes-Restrepo et al. (2014)) and the finite element methods (FEMs) (Bertrand et al., 1991; Piastra et al., 2018; Schimpf et al., 2002), the irregularity in the geometries does not pose a specific problem. In our study, we deal with FEM which requires a volumetric mesh where every element of the mesh can be represented as a hexahedron. The mesh can directly be extracted from a segmented MRI in which the lesion is specified as one of the tissue types. Each of the mesh elements is assigned with a conductivity that is based on the dominant tissue type of the corresponding voxels.

There are dedicated tools for the automatic segmentation of stroke lesions from MRI scans, avoiding the burden of manual work. In this study, we used LINDA (Pustina et al., 2016) in combination with meshing routines embedded in the FieldTrip toolbox (Oostenveld et al., 2011) to create a volumetric mesh.

There are several open-source tools that implement most of the analytic steps needed for source reconstruction pipelines, including the modeling of geometries with different levels of detail and complexity. Examples of such toolboxes are FieldTrip, Brainstorm (Tadel et al., 2011), and MNE-Python (Gramfort et al., 2013). Apart from offering (quasi-) analytical MEG solutions (Lalancette et al., 2011; Nolte, 2003), these toolboxes support BEM solutions through integration with the OpenMEEG toolbox (Gramfort et al., 2010). As already discussed, the level of detail we want to explore in this study extends beyond the limits dictated by BEM implementations that are readily available in open source tools; we are therefore interested in FEM solvers. Open-source FEM solvers are available for MEG forward solution computation like DUNEuro (Schrader et al., 2021) and SimBio (https://www.mrt.uni-jena.de/simbio). Here, we implement an analysis pipeline mainly based on FieldTrip, with the external computation of MEG leadfields implemented in DUNEuro-Python. The complete analysis pipeline is shared together with the present paper.

2. Materials and methods

In this section, we describe how we model the effects of lesions in MEG source reconstructions. The main steps are schematically visualized in Fig. 1.

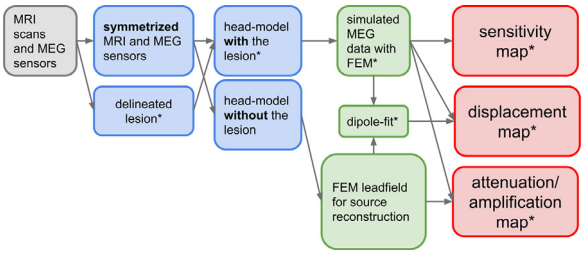

Fig. 1. Schematic representation of the main steps involved in our pipeline. Gray box: input data consisting of a T1w MRI scan, and MEG sensor position and orientation; Blue boxes: processing of input to create seven symmetrized headmodels, six with and one without the lesion, and sensors; Green boxes: MEG forward and inverse problem computation; Red boxes: output maps. We marked with asterisks the steps that are repeated for three different lesion sizes and three different lesion locations.

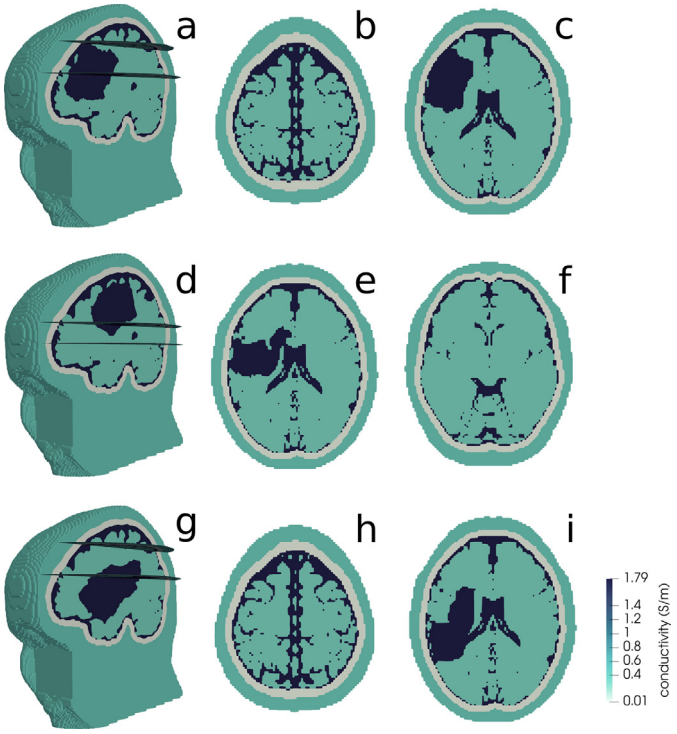

Fig. 2. Clipped symmetrized mesh (a,d,g) and the two axial slices considered in this study (center and right columns) for subject A (a,b,c), B (d,e,f) and C (g,h,i). For each subject we considered a slice crossing (c,e,i) and not crossing (b,f,h) the lesions. The colors follow the conductivity profile.

2.1. Data acquisition and selection

In this study, we used the anatomical data of three patients in the chronic phase of stroke (more than 1 year post-onset). The data were acquired under the approval of the Ethics Committee 'CMO regio Arnhem-Nijmegen' (NL58437.091.17) and the participants gave written informed consent. The subjects were scanned at the Donders Centre for Cognitive Neuroimaging with a 3T MAGNETOM PrismaFit scanner: a T1-weighted (T1w) MRI scan was acquired. The subjects also participated in a MEG study which was performed with a 275-channel MEG system (CTF-MEG, VSM MedTech Inc., Coquitlam, Canada). The MEG data itself is not used here, but we do use the head and sensor position information of this measurement. Out of a collection of 15 subjects' data already published (see Piastra et al. (2021a)), we selected three subjects whose lesions were similar in size (i.e., in a range from ≈ 90 and 110 ml) but different in location (i.e., from frontal to more posterior). See Fig. 2.

2.2. Modeling the head, the sources, and the sensors

We built seven different head models: one homogeneous head model, where the lesion is neglected, three head models with an incrementally larger lesion, and three head models with the lesion in different locations. To disentangle the effects on source reconstruction of normal and abnormal brain asymmetries and to reduce the anatomical differences between head models to the ones related to the lesions, we constructed head models that were explicitly made symmetric along the midline, starting from the MRI scan of one of the three patients, i.e., subject A. We describe the procedure in the following.

As the first step of our pipeline, we delineated the lesions of the three subjects using the LINDA toolbox (Pustina et al., 2016). LINDA is an R package for automatic segmentation of chronic stroke lesions based on machine learning algorithms. The input for LINDA is a T1w MRI scan, while the output is a volumetric description of the lesion.

After re-aligning and reslicing both the input MRI of subject A and the lesion volumes of subjects A,B and C produced by LINDA, we symmetrized the MRI scan of subject A by flipping the volumetric anatomical matrix of the non-lesioned hemisphere over the midline. The symmetrized MRI scan was segmented into four different components (brain, CSF, skull, and scalp), and the lesion volume was added as a fifth compartment. After this step, we had seven segmentations, one without, and the others with six different realistically shaped lesions. The six lesions were added to the same MRI flipped segmentation, the one from subject A. As to the lesion size, we eroded the lesion volume of subject A into two consecutive steps, in order to have two smaller lesions with the same shape as the one of subject A. In particular, the lesions are 1.5%, 5% and 9.5% of the brain volume, respectively. As to the lesion location, we considered the lesion of three different subjects, i.e., subject A, B, and C, and added them to the symmetrized segmentation of subject A. Axial sections of the six head models are visualized in Fig. 2. After downsampling the segmented volumes to a 2 mm resolution, we built hexahedral volumetric meshes, consisting of approximately 600K nodes and elements.

The conductivity for the non lesion tissues was assigned following the literature (brain = 0.33 S/m, CSF = 1.79 S/m, skull= 0.1 S/m and scalp = 0.43 S/m). The stroke lesions consist of a mixture of a CSF-filled cavity (the core) and injured gray and white matter in the vicinity of the cavity (the penumbra). While the CSF conductivity is known in the literature (Baumann et al., 1997; McCann et al., 2019), the conductivity of the penumbra is unknown. Following previous literature (e.g., Minjoli et al. (2017)), we modeled the lesion identified by LINDA as a CSF-filled cavity.

We modeled the sources as dipoles. To avoid numerical instability, the positions of the sources were chosen as the centroids of the elements in the mesh corresponding to brain tissue (excluding the lesion). For each dipole position, we considered three orthogonal source orientations.

The MEG helmet is constructed so that the MEG sensors are symmetrically distributed, but in the MEG experiment the subject's head does not need to be exactly in the middle of the helmet. To rule out left-right differences due to the asymmetric placement of the head in the helmet, we symmetrized the sensor positions by centering them on the head model.

2.3. MEG forward and inverse solutions

We created seven sets of forward models, based on the head model with and without the lesion. The six forward models with the lesions were used to simulate the sensor-level topographies that would have been recorded. The head model without the lesion was subsequently used in the source reconstruction to evaluate the effect of omitting the lesion. MEG forward solutions were computed applying a FEM with Lagrangian basis functions (Bertrand et al., 1991; Schimpf et al., 2002) and the so-called partial integration source modeling approach (Pursiainen

et al., 2012; Weinstein et al., 2000; Yan et al., 1991)) using the code implemented in the DUNEuro software (Schrader et al., 2021), validated in Piastra et al. (2018), and made available in the Donders Repository (https://doi.org/10.34973/92gd-3235).

For the simulated MEG scalp topography corresponding to each source, we computed a dipole scan fitting one dipole using the FieldTrip toolbox (Scherg, 1990) in the head model with the lesion.

2.4. Evaluating the effect of omitting the lesion on source reconstruction results

We quantified the lesion effect with three different maps: sensitivity, displacement, and attenuation/amplification. This was repeated for the six head models and three axial slices for each model. Two of these slices intersected the lesion, and one slice was located approximately 20 mm above or below the lesion. We visualized the slices color-coded with each of these three measures. The slices of interest and their location in relation to the lesion and head are shown in Fig. 2. Since the two slices crossing the lesion lead to similar results, we present here the analysis relative only to one of the two crossing axial planes.

2.4.1. Sensitivity maps

The amplitude of the sensor-level MEG signal varies with the location and orientation of the source, even if the source amplitude is kept constant. MEG is known to be considerably less sensitive to radially oriented sources compared to tangential sources, and to deep sources compared to superficial sources (e.g., Piastra et al. (2021b)). This inherent variability in MEG sensitivity needs to be taken into account. We therefore quantified sensitivity maps for the simulated sources to the computed MEG signal. For every dipole we computed the mean over channels of the forward solution normalized by its maximum, i.e.,

$$sens_i = avg_i / max_{i=1,\ldots,Ndip}(sens_i), \tag{1}$$

where

$$avg_i = 1/Nch \cdot \sum_{j=1}^{Nch} |sol(i,j)|. \tag{2}$$

for every dipole i, $i = 1, \ldots, Ndip$ and every channel j, $j = 1, \ldots, Nch$. $sol(i,j)$ is the MEG forward solution corresponding to the i-th dipole and the j-th channel; $Ndip$ is the number of dipoles; Nch is the number of MEG channels. The MEG sensitivity is expressed in percent for each dipole location and visualized to aid in the interpretation of the remainder of our results.

2.4.2. Displacement maps

One effect of neglecting the asymmetry due to the lesion when performing source reconstruction is the dipole localization error, which can be quantified in mm. Using the model without the lesion, we fitted dipoles to the forward model topographies that were created using the head model with the lesion. We computed the displacement as the Euclidean distance between the original dipole location, and the reconstructed location.

2.4.3. Attenuation/amplification maps

Another error that can result from neglecting the asymmetry due to the lesion is that the amplitude of the activity is estimated incorrectly. We computed the ratio (in dB) between the MEG topography from the head model with the lesion and the one from the head model without the lesion, for each dipole position and dipole orientation in each of the three axial slices. The attenuation/amplification value for the dipole in the i-th original location is quantified by

$$a_i = 10 * log_{10}(diag(pinv(topography\_with_i) * topography\_without_i)), \tag{3}$$

where $topography\_with_i$ and $topography\_without_i$ are the forward solutions computed when the lesion is included or not in the model, respectively. In particular, the product $pinv(topography\_with_i) * topography\_without_i)$ gives a 3×3 matrix where on the diagonal are the ratios between leadfields from the head model with the lesion and the ones without. The first element of the diagonal of such matrix stands for the ratio in the x-axis, the second for the ratio in the y-axis and the third for the ratio in the z-axis.

From Eq. 3 we see that the value of a_i in dB is negative in the case of attenuation, i.e., when $topography\_without_i$ is smaller than $topography\_with_i$; vice versa, a_i is positive (i.e., there is signal amplification) when $topography\_without_i$ is bigger than $topography\_with_i$.

3. Results

We present the results considering the effects of lesion size, location and distance for each of the three maps computed, i.e., sensitivity, displacement and attenuation-amplification.

3.1. Sensitivity maps

The sensitivity maps need to be considered for the interpretation of the following results (i.e., displacement and attenuation/amplification maps). In particular, areas with a low a priori sensitivity might be prone to larger displacement errors which are not due to forward modeling inaccuracies, as we will see in detail in the next section.

3.1.1. Size effects

Figure 3 shows the sensitivity maps for dipoles pointing into the x-direction (posterior to anterior axis, leftmost column), the y-direction (left to right axis, central column), and z-direction (inferior to superior axis, rightmost column) for different lesion sizes (top-down). In general, we see that, as expected from literature (e.g., Piastra et al. (2021b)), the sensitivity is largest (up to 100%) for superficial tangential dipoles, and rapidly decreases for deeper dipoles. The closer the dipole is to the center of the head, the weaker the sensitivity of the MEG becomes. For x-oriented dipoles (left column), tangential dipoles are on the outer left and right contours of the left and right hemispheres, respectively; for y-oriented dipoles (center column), tangential dipoles are mainly in the anterior and posterior areas; for z-oriented dipoles (right column), tangential dipoles, and corresponding brighter colors in the map, follow the whole contour of the slices and concentric isolines are visible. This behaviour becomes clearer in the sphere simulation study in the Supplementary Material.

From Fig. 3, we see that the symmetry of the maps becomes more disrupted the larger the lesions. This effect is especially notable along the dipole orientation axis. In particular, when looking at the sensitivity maps for y-axis oriented dipoles in Fig. 3(b,e,h), we can see that areas between the center of the brain slice, i.e., ventricles, and the lesion have higher sensitivity for bigger lesions. Similarly, for the same dipoles, the contralesional hemisphere appears more sensitive as well, i.e., the areas with the lowest sensitivity are shrunk. Overall, we see that there is higher sensitivity for bigger lesions (cfr. Supplementary Material).

3.1.2. Location effects

In Fig. 4, we visualized the sensitivity maps for x- (left column), y-(central column) and z-oriented dipoles (right column) corresponding to head models where lesions are positioned differently in the brain compartment that is, lesions delineated from subject A (a,b,c), subject B (d,e,f) and subject C (g,h,i). From Fig. 4, we see a disrupted sensitivity symmetry caused by the lesion. This effect seems to be independent from the lesion location, and it can be seen more evidently in the sphere simulations in the Supplementary Material.

3.1.3. Distance effects

In Fig. 5, we see that the effects of the presence of the lesion can still be captured by the maps even when 20 mm away from the lesions. This

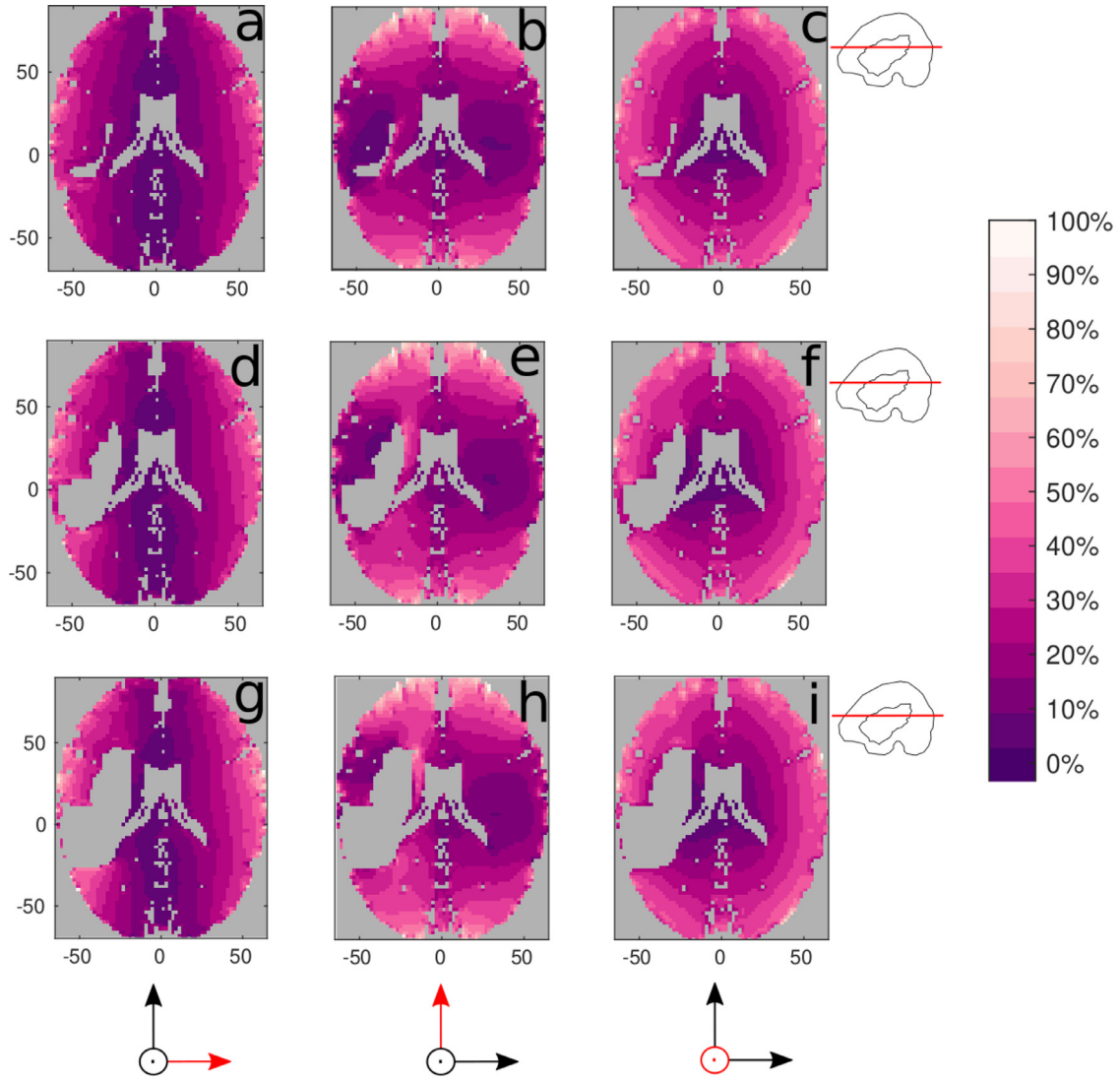

Fig. 3. MEG sensitivity map in percentage relative to x- (a,d,g), y- (b,e,h), and z-oriented (c,f,i) original dipoles in one slice crossing the lesion, for increasing lesion sizes (top to bottom). A schema representing the contour of the inner skull compartment, the lesion and the cutting axial plane (in red) is visualized on the right. In each dipole position, the mean over channels is normalized by the maximum. Brighter pixels stand for high sensitivity, dark purple pixels for low sensitivity. Note the MRI coordinate system (in mm) shown in the axes. Dipoles orientations are schematically indicated at the bottom of the figure.

is particularly evident in Fig. 5(c,i,d,e), where the sensitivity is higher right above (c,i) or below (d,e) the lesion.

The z-level of the slice and the distance to the sensors indeed play a role. Dipoles lying on the midline turn out to be tangential, since they are closer to the upper surface of the head and are therefore visible with MEG. We also notice high sensitivity values for dipoles lying in the upper slice, z-oriented, and located in posterior areas.

3.2. Displacement maps

Figure 6 shows the dipole displacements (on the left) and the MEG sensitivity map (on the right) for subject A in one axial slice crossing the lesion. Overall, large displacements are observed along the symmetry axis on which they are oriented. For example, for x-oriented dipoles (toward the nose), maximum displacement values up to 50 mm are along the x-axis, i.e., the head midline (see Fig. 6(a)). In addition, z-oriented dipoles (toward the vertex) located in posterior areas show displacement values around 30 mm. The dipole displacement is not symmetrically distributed; the highest displacement values are observed close to the lesion. This effect is especially noticeable in Fig. 6(a) and (c), where we see a cluster of dipoles between the lesion and the center of the brain exhibiting high displacement values. A similar asymmetrical cluster is visible above the lesion in Fig. 6(c), for z-oriented dipoles.

The sensitivity maps shown in Fig. 6(d,e,f) guide the interpretation of the displacement maps. We can see that the displacements peaks, i.e., above 30 mm, are present in areas where the sensitivity is below 20%. Nevertheless, we can also notice that there are areas where the sensitivity is above 45% and the displacement is above 15 mm. One example of this can be seen in Fig. 6(b) and (e). In the brain tissue between the lesion and the ventricles, we notice 10 mm displacement and more than 85% sensitivity.

3.2.1. Size effects

In general, from Fig. 7 we notice that highest displacement values are concentrated around the lesion. In addition, we can see that displacement values get higher for larger lesions. In particular, for the biggest lesion (Fig. 7(g,h,i)), which corresponds to the actual lesion of subject A, we see that, despite being low, displacement values are also found in the contralesional hemisphere. Particularly high displacement values, i.e., up to 45 mm, are visible in the perilesional area confined between the ventricles and the lesion, especially high for x-oriented dipoles (Fig. 7(g)). This effect becomes more visible in the sphere simulations.

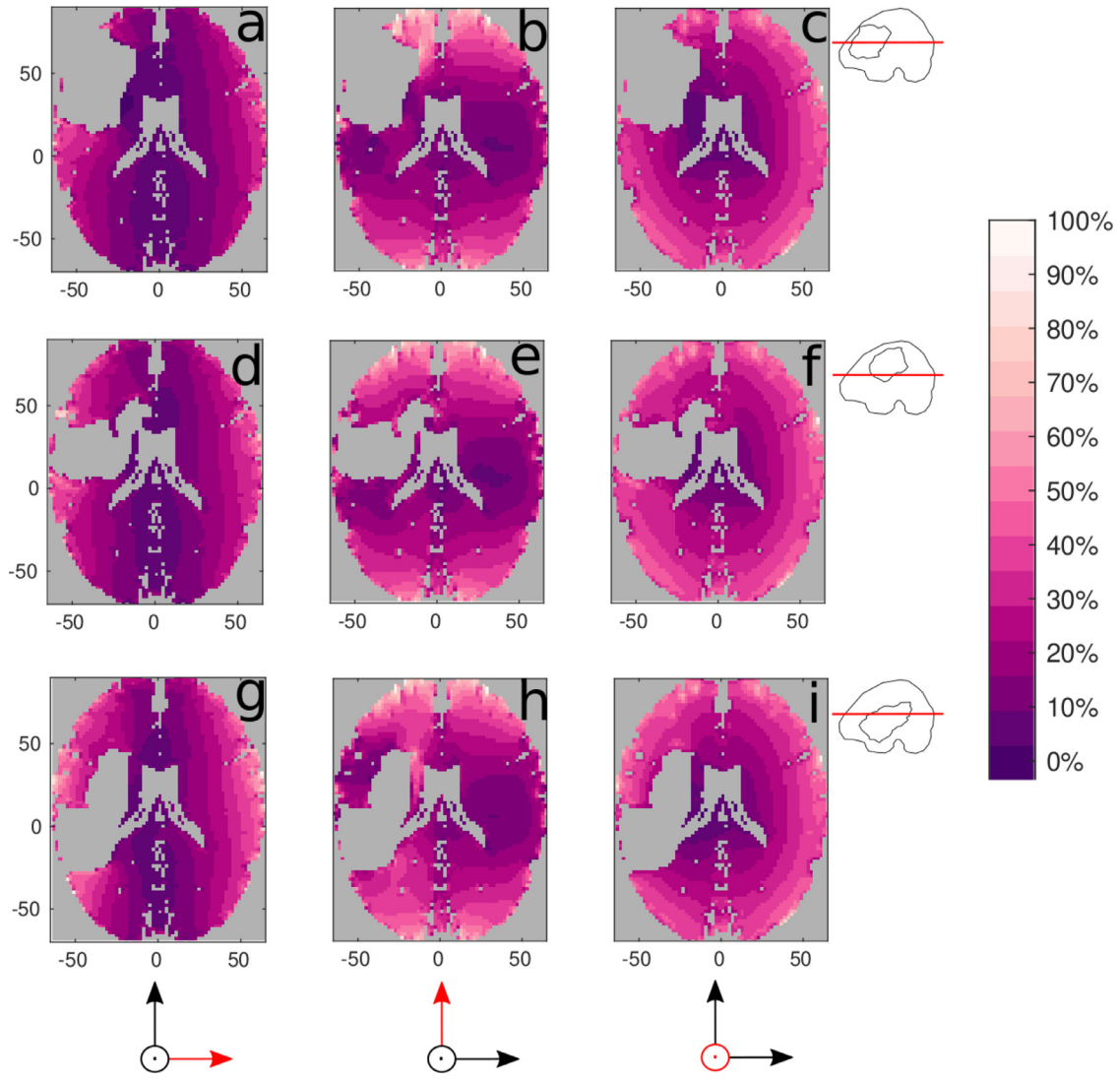

Fig. 4. MEG sensitivity map in percentage relative to x- (a,d,g), y- (b,e,h), and z-oriented (c,f,i) original dipoles in one slice crossing the lesion, for different lesion locations, i.e., anterior (a,b,c), middle and medial (d,e,f), middle and posterior (g,h,i) lesions. A schema representing the contour of the inner skull compartment, the lesion and the cutting axial plane (in red) is visualized on the right. In each dipole position, the mean over channels is normalized by the maximum. Brighter pixels stand for high sensitivity, dark purple pixels for low sensitivity. Note the MRI coordinate system (in mm) shown in the axes. Dipoles orientations are schematically indicated at the bottom of the figure.

3.2.2. Location effects

In Fig. 8, we see high displacement values in the perilesional areas, independently from the location of the lesion (different rows of Fig. 8). As already noticed in Fig. 7(g,h,i), displacement values are found also in the contralesional hemisphere. Note that the lesion size does not change in this comparison.

3.2.3. Distance effects

In Fig. 9, we see that the effects of having the lesion in the head model are still strong in areas that are around 20 mm away from the lesion and where the sensitivity is not so low. This effect is particularly visible in Fig. 9(c) and f, for z-oriented dipoles. In the ipislesional hemisphere, there are displacement values up to 20mm where the sensitivity is over 70%.

3.3. Attenuation/amplification maps

3.3.1. Size effects

Figure 10 shows the attenuation/amplification maps for different lesion sizes (top to bottom). These are not symmetric and show non-negligible amounts of attenuation and amplification around the lesion. For dipoles radial and close to the lesion, we see amplification effects (red clusters), while for dipoles tangential and close to the lesion, there are attenuation effects (blue clusters). This is confirmed in the sphere simulations in the Supplementary Material. In addition, we notice stronger and wider amplification/attenuation effects with increasing lesion size.

3.3.2. Location effects

From Fig. 11, we see high attenuation and amplification values around the lesion, with the same orientation mentioned above: amplification effects for dipoles radial and close to the lesion, and attenuation effects for tangential dipoles.

3.3.3. Distance effects

Amplification and attenuation effects are also visible when considering a slice 20 mm away from the lesion, as seen in Fig. 12(a,b,c). In the same areas, the sensitivity reaches up to 80%, similarly to what was already seen for the displacement results.

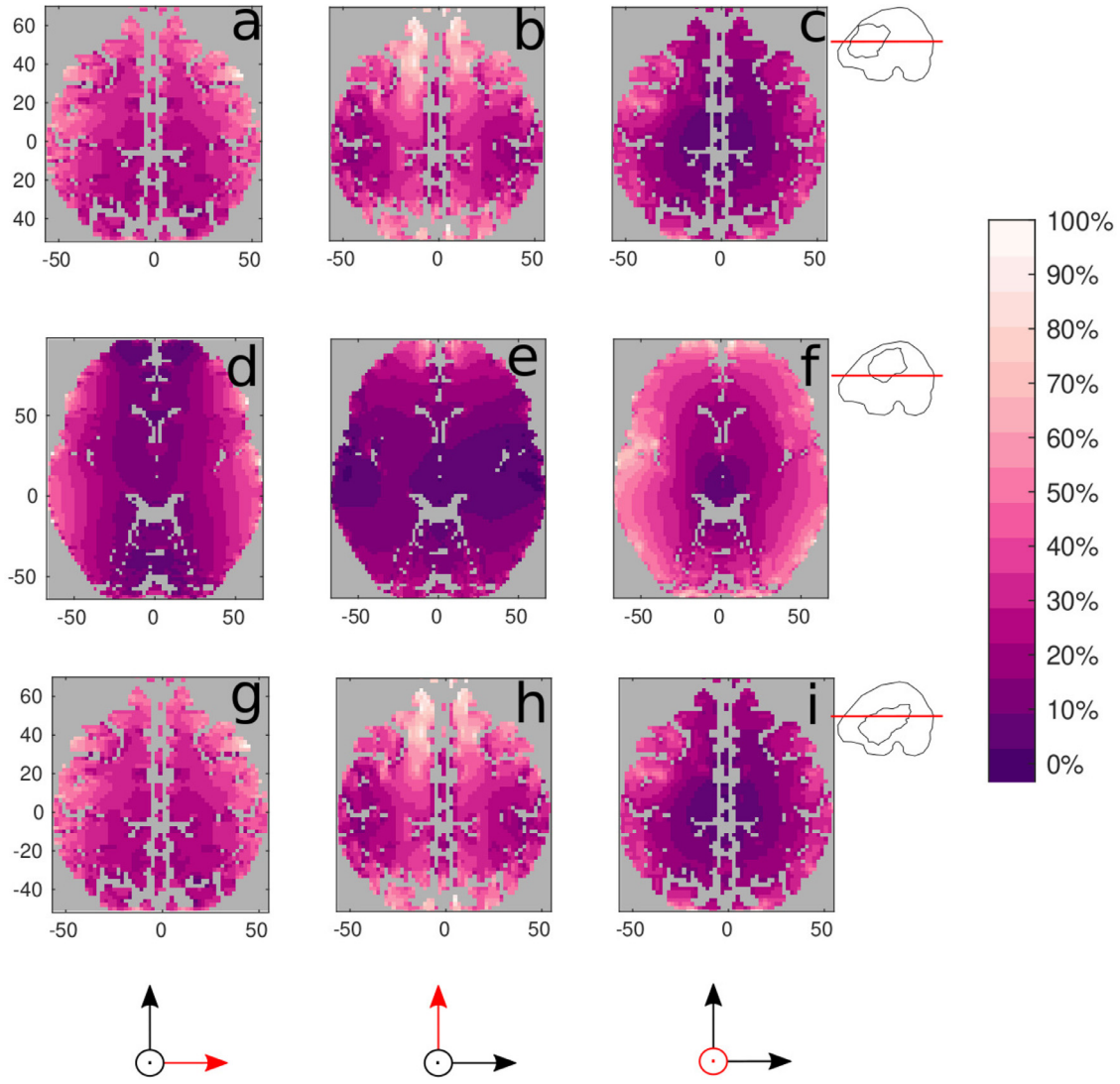

Fig. 5. MEG sensitivity map in percentage relative to x- (a,d,g), y- (b,e,h), and z-oriented (c,f,i) original dipoles in one slice away from the lesion, i.e., above (a,b,c,g,h,i) and below (d,e,f) for different lesion locations, i.e., anterior (a,b,c,g,h,i), middle and medial (d,e,f), middle and posterior (g,h,i) lesions. A schema representing the contour of the inner skull compartment, the lesion and the cutting axial plane (in red) is visualized on the right. In each dipole position, the mean over channels is normalized by the maximum. Brighter pixels stand for high sensitivity, dark purple pixels for low sensitivity. Note the MRI coordinate system (in mm) shown in the axes. Dipoles orientations are schematically indicated at the bottom of the figure.

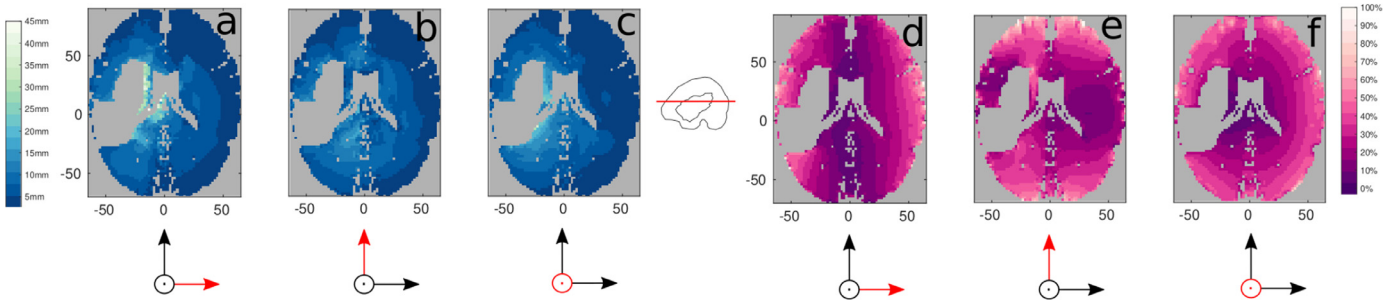

Fig. 6. Left: Dipole-fit displacement map relative to x- (a), y- (b), and z-oriented (c) original dipoles for subject A in one axial slice crossing the lesion. In each dipole position, the magnitude of the vector difference between the original dipole location and the reconstructed dipole location is visualized in the original dipole location. Brighter pixels stand for high displacement, blue pixels for low displacement. Note that the colormap was clipped at 45 mm for visualization purposes. Right: MEG sensitivity map in percentage relative to x- (d), y- (e), and z-oriented (f) original dipoles for subject A in one axial slice crossing the lesion. In each dipole position, the mean over channels is normalized by the maximum. Brighter pixels stand for high sensitivity, dark purple pixels for low sensitivity. Note the MRI coordinate system (in mm) shown in the axes. Dipoles orientations are schematically indicated at the bottom of the figure. A schema representing the contour of the inner skull compartment, the lesion and the cutting axial plane (in red) is visualized in the center.

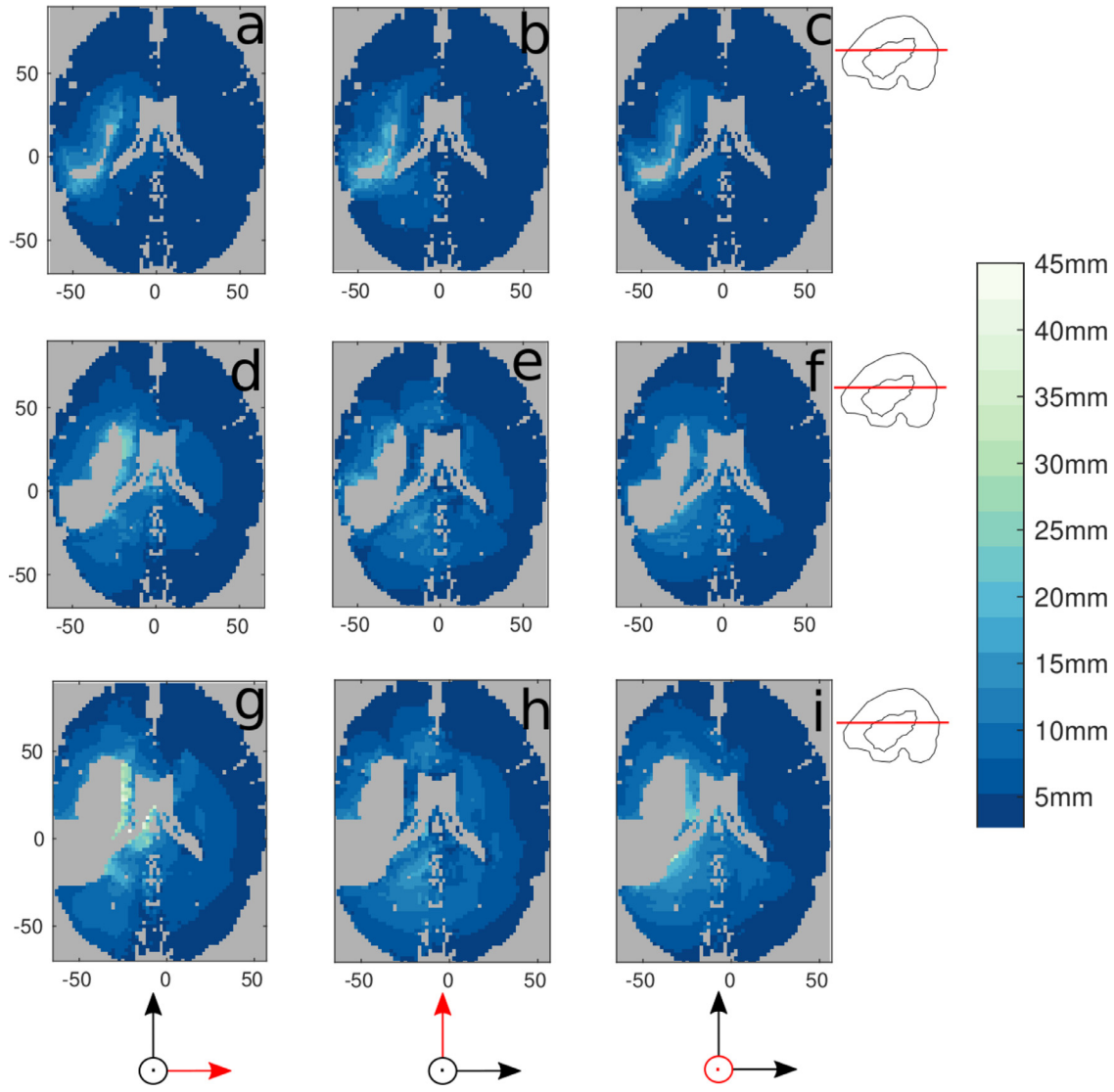

Fig. 7. Dipole-fit displacement map relative to x- (a,d,g), y- (b,e,h), and z-oriented (c,f,i) original dipoles in one slice crossing the lesion, for increasing lesion sizes (top to bottom). A schema representing the contour of the inner skull compartment, the lesion and the cutting axial plane (in red) is visualized on the right. In each dipole position, the magnitude of the vector difference between the original dipole location and the reconstructed dipole location is visualized in the original dipole location. Brighter pixels stand for high displacement, blue pixels for low displacement. Note that the colormap was clipped at 45 mm for visualization purposes. Dipoles orientations are schematically indicated at the bottom of the figure.

4. Discussion

In this study, we simulated and analyzed the effects of not including a chronic stroke brain lesion in the head model when performing MEG source reconstruction. For this, we computed displacement maps to quantify the distribution of localization errors and attenuation/amplification maps to quantify the errors in estimated source amplitude, while including the lesion model for the forward solution and neglecting it for the inverse solution. In addition, general MEG sensitivity maps guided the interpretation of these maps. We additionally studied the influence of lesion size and location both in realistically shaped head models and in spherical models (see Supplementary Materials).

We found high displacement and attenuation/amplification values asymmetrically located around the lesion, even for dipoles approximately 20 mm away from the lesion. Although the MEG sensitivity is not the highest for these dipoles, these cortical areas are accessible in MEG studies. Bigger lesions lead to stronger effects impacting larger areas, independently from the lesion location. Some of these effects become clearer in the simplified scenarios analyzed in the Supplementary Material with sphere models.

Our results highlight that care is required in the interpretation of source reconstruction results when studying sources that are close and radial to the lesion, for which we observed amplification effects of up to 5 dB. Especially delicate is the scenario where these sources happen to be superficial, as we saw for example, in the z-oriented dipoles 20 mm above the posterior part of the lesion (Fig. 12(c)). In these cases, the MEG sensitivity is high and bigger effects are expected in source reconstruction results.

From the displacement maps (Fig. 6), we see high displacement values (up to 50 mm) along the corresponding dipole-orientation axis. This can be explained by the fact that a similar pattern is found in the sensitivity maps with an opposite trend, i.e., the sensitivity is low for deep dipoles lying in their orientation axis. In particular, it is reasonable to assume that low norms of the leadfields cause the dipole-fit algorithm to be more sensitive to small numeric discrepancies between the two sets of leadfields, resulting in large displacement values. This effect can be compared to the effect of adding noise (i.e., decreasing the signal-to-noise

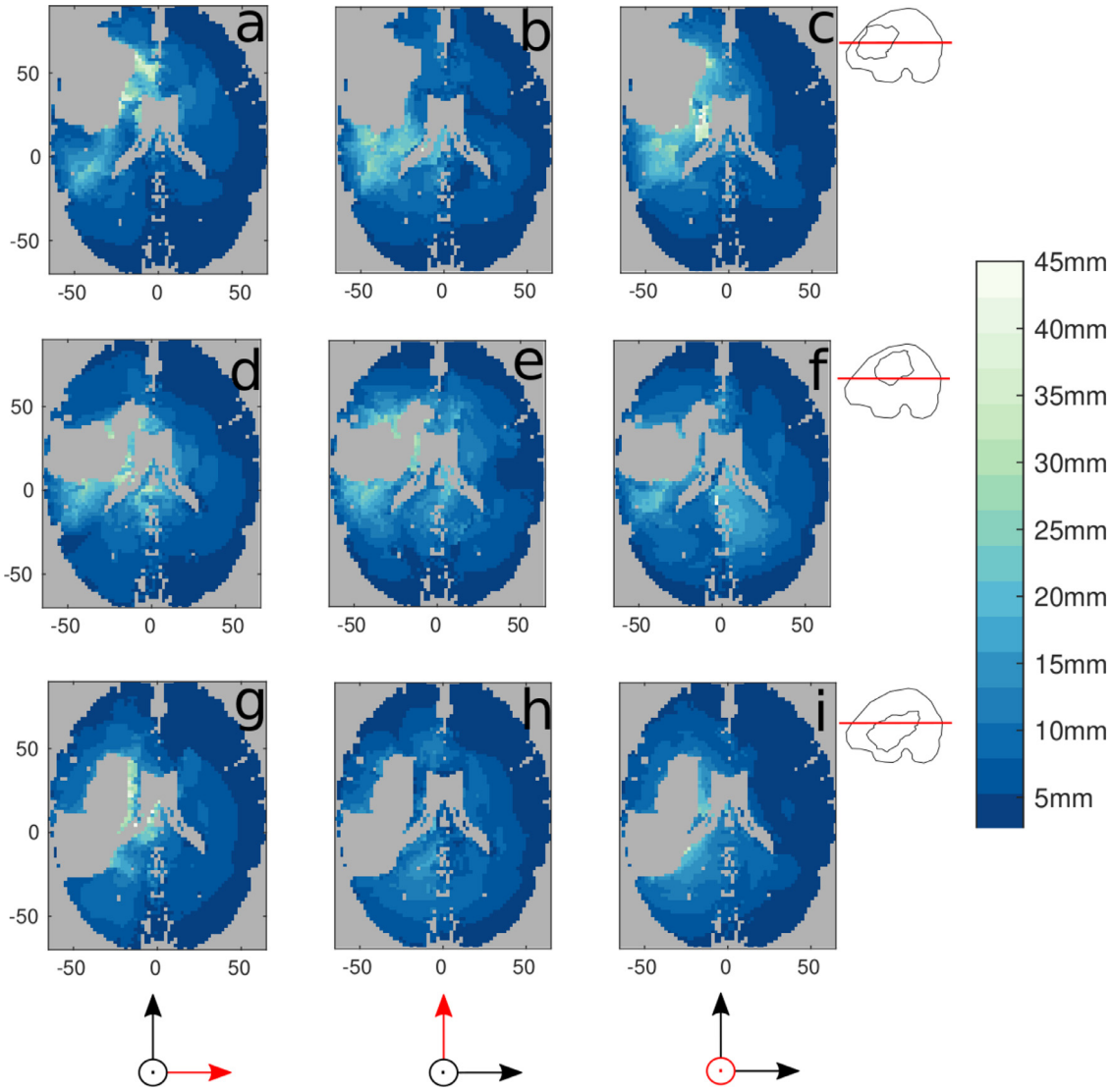

Fig. 8. Dipole-fit displacement map relative to x- (a,d,g), y- (b,e,h), and z-oriented (c,f,i) original dipoles in one slice crossing the lesion, for different lesion locations, i.e., anterior (a,b,c), middle and medial (d,e,f), middle and posterior (g,h,i) lesions. A schema representing the contour of the inner skull compartment, the lesion and the cutting axial plane (in red) is visualized on the right. In each dipole position, the magnitude of the vector difference between the original dipole location and the reconstructed dipole location is visualized in the original dipole location. Brighter pixels stand for high displacement, blue pixels for low displacement. Note that the colormap was clipped at 45 mm for visualization purposes. Dipoles orientations are schematically indicated at the bottom of the figure.

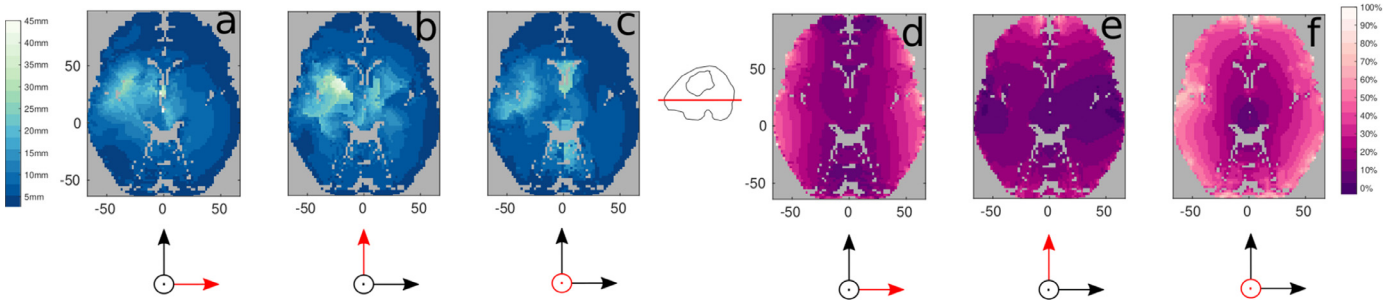

Fig. 9. Left: Dipole-fit displacement map relative to x- (a), y- (b), and z-oriented (c) original dipoles for subject A in one axial slice not crossing the lesion. In each dipole position, the magnitude of the vector difference between the original dipole location and the reconstructed dipole location is visualized in the original dipole location. Brighter pixels stand for high displacement, blue pixels for low displacement. Note that the colormap was clipped at 45 mm for visualization purposes. Right: MEG sensitivity map in percentage relative to x- (d), y- (e), and z-oriented (f) original dipoles for subject A in one axial slice not crossing the lesion. In each dipole position, the mean over channels is normalized by the maximum. Brighter pixels stand for high sensitivity, dark purple pixels for low sensitivity. Note the MRI coordinate system (in mm) shown in the axes. Dipoles orientations are schematically indicated at the bottom of the figure. A schema representing the contour of the inner skull compartment, the lesion and the cutting axial plane (in red) is visualized in the center.

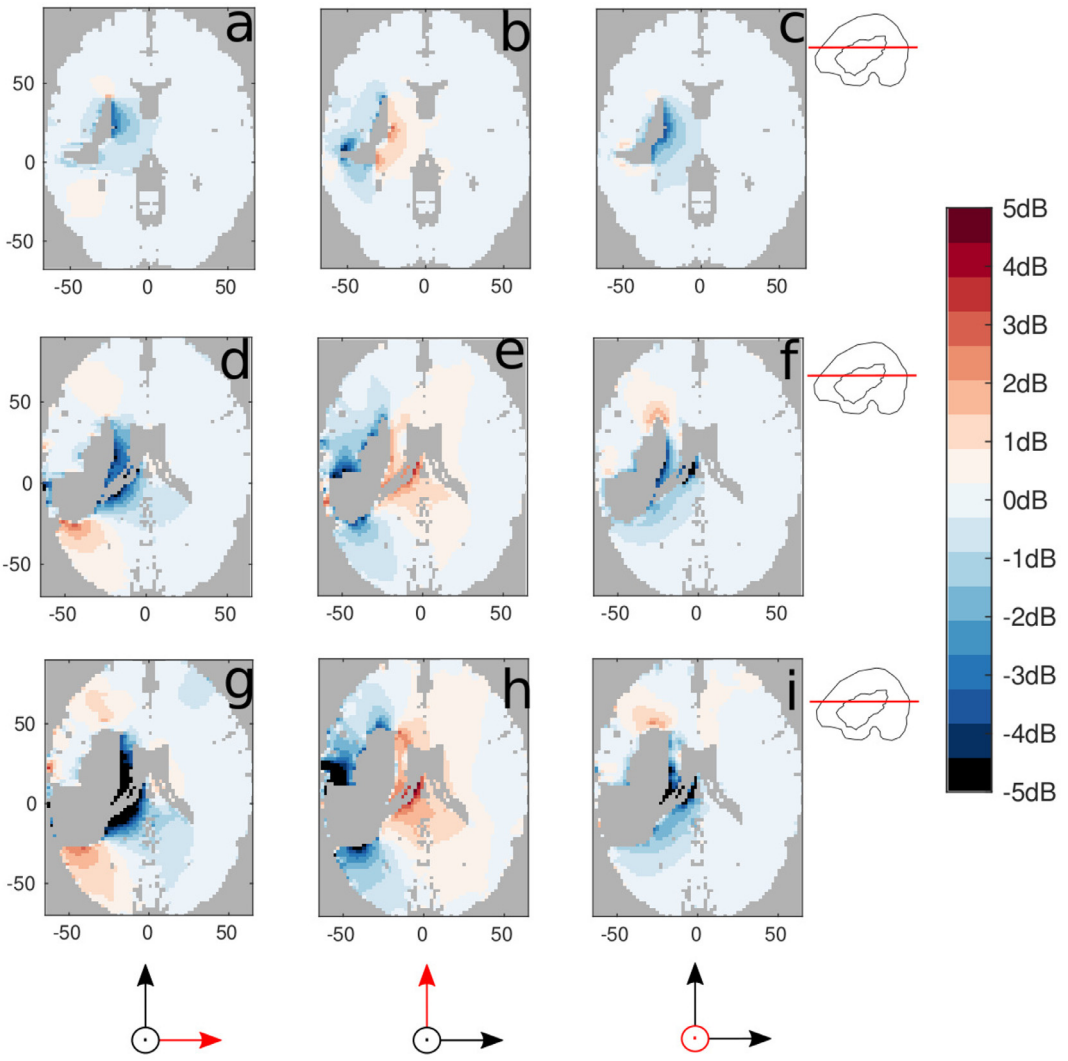

360

Fig. 10. Attenuation/amplification map relative to x- (a,d,g), y- (b,e,h), and z-oriented (c,f,i) original dipoles in one slice crossing the lesion, for increasing lesion sizes (top to bottom). A schema representing the contour of the inner skull compartment, the lesion and the cutting axial plane (in red) is visualized on the right. In each dipole position, the ratio between the leadfield relative to the head model without and with the lesion (in dB and centered around the value 0) is visualized in the original dipole location. Blue pixels stand for attenuation, red pixels for amplification, white pixels for neither amplification nor attenuation. Note that the colormap was clipped between 5 and -5 dB. Note the MRI coordinate system (in mm) shown in the axes. Dipoles orientations are schematically indicated at the bottom of the figure.

ratio), which leads to higher localization errors (e.g., Cuffin (1986)) and, here, adds to the discrepancy between the measured topography (i.e., simulated MEG data, with the lesion), and the model topography (i.e., without the lesion).

The stroke lesion taken into account in this study can be considered an illustration of a more general phenomenon, i.e., localized brain asymmetric volumes, filled with CSF. It is reasonable to assume that in cases of surgically resected brain areas in epilepsy and brain tumors, similar source localization effects might occur.

When considering different types of localized brain asymmetries, i.e., brain tumors and cerebral edemas that are caused for example by traumatic brain injury (e.g., concussions), the conductivity might be very different and therefore influence the displacement and attenuation/amplification maps. In our case, we model the stroke lesion as a CSF-filled cavity and thus assign it the high conductivity of the CSF. The CSF is the most conductive physiological material in the human head and leads to strong electric current channeling and deviations (e.g., Piastra et al. (2021b)).

Our study has a number of limitations. Following other examples in the literature (see, for example, Minjoli et al. (2017)), we modeled the stroke lesion as a CSF-filled cavity. It is nevertheless visible from the MRI of other patients (see, for example, Fig. 1A, upper subfigure, in Minjoli et al. (2017)) that the effects of chronic stroke on the head are not only to create a cavity (stroke core area) but also to injure brain tissues usually surrounding the cavity. In our simulations, we treated the former (but not the latter) as CSF. Assigning the high conductivity of CSF to the CSF-filled cavity of the core lesion might not be realistic though, as it represents the most extreme scenario and even the CSF-filled cavity may still contain small portions of mixed tissue otherwise not easily visible in a T1-weighted MRI. Therefore, here, similarly to what is done in Stenroos and Hauk (2013), we are taking into account the worst-case scenario, that is, we are indeed assigning to the lesion volume the conductivity of the CSF, i.e., the highest in the head model, to the extent that the voxels in the lesion volume were segmented by the segmentation tool as CSF. Some effects might be therefore overestimated with respect to other patients' data. Nevertheless, we expect the overestimation to be only minor, if compared with the effects of not including the lesion in the model at all. Another limitation might be due to the process of symmetrizing the head model that was not optimal. From Fig. 2, first slice on the left, we can see artificial and non-realistic

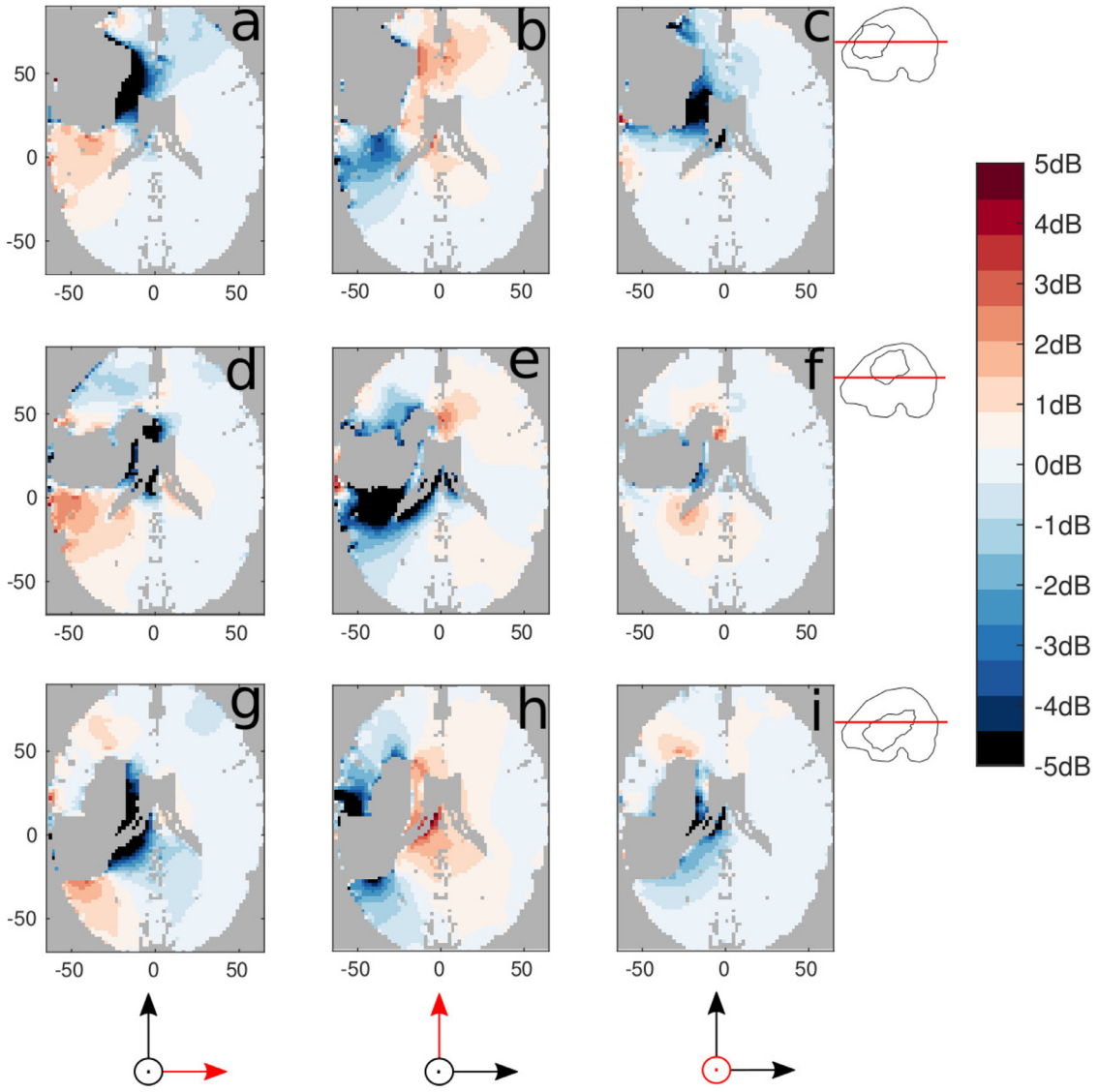

Fig. 11. Attenuation/amplification map relative to x- (a,d,g), y- (b,e,h), and z-oriented (c,f,i) original dipoles in one slice crossing the lesion, for different lesion locations, i.e., anterior (a,b,c), middle and medial (d,e,f), middle and posterior (g,h,i) lesions. A schema representing the contour of the inner skull compartment, the lesion and the cutting axial plane (in red) is visualized on the right. In each dipole position, the ratio between the leadfield relative to the head model without and with the lesion (in dB and centered around the value 0) is visualized in the original dipole location. Blue pixels stand for attenuation, red pixels for amplification, white pixels for neither amplification nor attenuation. Note that the colormap was clipped between 5 and -5 dB. Note the MRI coordinate system (in mm) shown in the axes. Dipoles orientations are schematically indicated at the bottom of the figure.

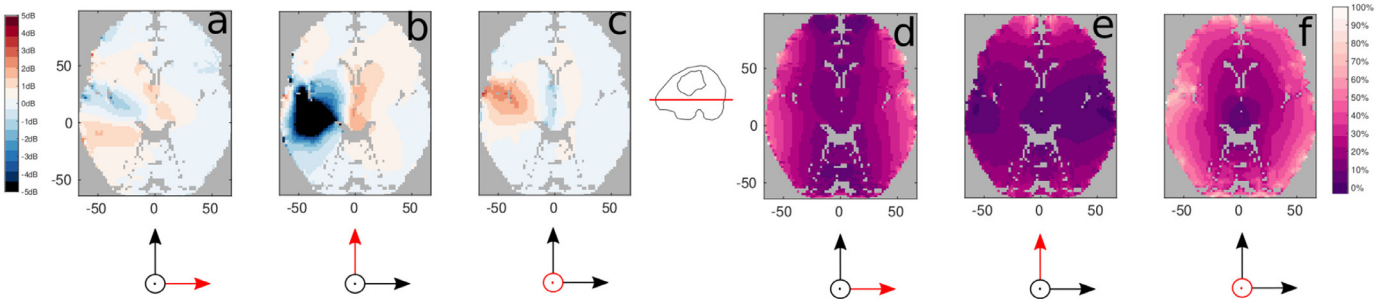

Fig. 12. Left: Attenuation/amplification map relative to x- (a), y- (b), and z-oriented (c) original dipoles in one axial slice not crossing the lesion. In each dipole position, the ratio between the leadfield relative to the head model without and with the lesion (in dB and centered around the value 0) is visualized in the original dipole location. Blue pixels stand for attenuation, red pixels for amplification, white pixels for neither amplification nor attenuation. Note that the colormap was clipped between 5 and -5 dB. Right: MEG sensitivity map in percentage relative to x- (d), y- (e), and z-oriented (f) original dipoles for subject A in one axial slice not crossing the lesion. In each dipole position, the mean over channels is normalized by the maximum. Brighter pixels stand for high sensitivity, dark purple pixels for low sensitivity. Note the MRI coordinate system (in mm) shown in the axes. Dipoles orientations are schematically indicated at the bottom of the figure. A schema representing the contour of the inner skull compartment, the lesion and the cutting axial plane (in red) is visualized in the center.

segmented tissue along the midline in the inter-hemispheric areas. A possible strategy to improve this is to use an affine co-registration of the flipped MRI to the original MRI and compute the average between the two volumes. This procedure is used when creating brain atlases (see, for example, Tona et al. (2017)). Nevertheless, we do not think that a better-symmetrized head model would have changed our findings. Furthermore, in this analysis, we did not explicitly simulate noise. The study presented here focuses on quantifying the effect of a lesion on the source estimate (location, orientation, and amplitude). Since we found that these effects can be sizable, a possible follow-up analysis might involve in-detail analyses of source reconstruction results of real data with regards to different signal-to-noise-ratios, which can therefore be quantified with measures like goodness-of-fit.

Additional studies could also focus on using different conductivity values assigned to the core-lesion and their impact on the source localization, analogously to what we partially explored in Piastra et al. (2021a). Similarly, given that the focus of our study was not on comparing source reconstruction techniques, future studies would need to address this issue.

Modeling lesions poses some technical challenges. The geometrical resolution of the imaging data of the patient should be high enough. Segmentation tools are able to segment CSF-filled cavities, therefore volumetric meshes are relatively easy to build. Building a volumetric mesh from an MRI is well supported in various open source and easy-to-use pipelines. One of the solvers that can take more sophisticated geometries into consideration is FEM. FEM implementations are openly distributed in the community, but still not easily accessible to a broader audience. Nevertheless, some first attempts have been carried out, for example, to facilitate the usage of DUNEuro for MEG solutions. Further efforts in distributing the code might be beneficial to a wider audience. In theory, BEM approaches would also be able to take lesions into consideration (see, e.g., Stenroos (2016), Kybic et al. (2006)). Nevertheless, in practice, it requires more effort to build the geometry in this case, since the most distributed implementation of BEM requires non-intersecting superficial meshes, which are not straightforward to create.

5. Conclusions

Brain lesions that lead to asymmetrically distributed CSF-filled cavities should be modeled when performing MEG source reconstruction, independently from the lesion location. This is particularly important when investigating deep sources or functions associated with lateralized brain activity, and the lesion is around 10% or more of the whole brain volume. The strongest effects of a CSF-filled stroke lesion, both in terms of displacement of the reconstructed sources as well as the strength of the source, are visible not only in perilesional areas but can extend up to 20 mm from the lesion. Higher priority should be given to the implementation and accessibility of FEM solvers, to extend the possibility for clinical neuroimaging researchers with less technical expertise to improve the interpretation of the patients MEG data.

Data and code availability statement

The data and code that support the findings of this study are available from the Donders Repository (https://doi.org/10.34973/92gd-3235).

Credit authorship contribution statement

Maria Carla Piastra: Conceptualization, Formal analysis, Methodology, Project administration, Software, Writing – original draft, Writing – review & editing, Visualization. **Robert Oostenveld:** Conceptualization, Methodology, Writing – review & editing, Supervision. **Jan Mathijs Schoffelen:** Conceptualization, Software, Writing – review & editing, Visualization. **Vitória Piai:** Conceptualization, Writing – review & editing, Supervision, Project administration, Funding acquisition.

Acknowledgments

MCP was supported by a grant from the Applied and Engineering Science domain (TTW) of the Netherlands Organization of Scientific Research (NWO): NeuroCIMT-iTDCS (Grant No. 14902) and by the FLAG-ERA grant NeuronsReunited (NWO Grant No. 680-91-318). JMS was supported by an NWO Vidi grant (864-14-011). VP was supported by an NWO Veni grant (451-17-003). We thank Simon Homölle and Thom Oostendorp for their input.

Supplementary material

Supplementary material associated with this article can be found, in the online version, at doi:10.1016/j.neuroimage.2022.119422

References

Baumann, S.B., Wozny, D.R., Kelly, S.K., Meno, F.M., 1997. The electrical conductivity of human cerebrospinal fluid at body temperature. IEEE Trans. Biomed. Eng. 44 (3), 220–223.

Bénar, C., Gotman, J., 2002. Modeling of post-surgical brain and skull defects in the EEG inverse problem with the boundary element method. Clinical Neurophysiology 113 (1), 48–56.

Bertrand, O., Thevenet, M., Perrin, F., 1991. 3D finite element method in brain electrical activity studies. In: Biomagnetic localization and 3D Modeling, pp. 154–171.

Brette, R., Destexhe, A., 2012. Handbook of neural activity measurement. Cambridge University Press.

Cook, M.J., Koles, Z.J., 2006. A high-resolution anisotropic finite-volume head model for EEG source analysis. In: 2006 International Conference of the IEEE Engineering in Medicine and Biology Society. IEEE, pp. 4536–4539.

Cuffin, B.N., 1986. Effects of measurement errors and noise on MEG moving dipole inverse solutions. IEEE Trans. Biomed. Eng. 9, 854–861.

Dannhauer, M., Lanfer, B., Wolters, C.H., Knösche, T.R., 2011. Modeling of the human skull in EEG source analysis. Hum Brain Mapp 32 (9), 1383–1399.

Datta, A., Baker, J.M., Bikson, M., Fridriksson, J., 2011. Individualized model predicts brain current flow during transcranial direct-current stimulation treatment in responsive stroke patient. Brain Stimul 4 (3), 169–174.

Douiri, A., Rudd, A.G., Wolfe, C.D., 2013. Prevalence of poststroke cognitive impairment: South London stroke register 1995–2010. Stroke 44 (1), 138–145.

Duncan, J.S., Winston, G.P., Koepp, M.J., Ourselin, S., 2016. Brain imaging in the assessment for epilepsy surgery. The Lancet Neurology 15 (4), 420–433.

Gramfort, A., Luessi, M., Larson, E., Engemann, D.A., Strohmeier, D., Brodbeck, C., Goj, R., Jas, M., Brooks, T., Parkkonen, L., et al., 2013. MEG and EEG data analysis with MNE-Python. Front Neurosci 7, 267.

Gramfort, A., Papadopoulo, T., Olivi, E., Clerc, M., 2010. OpenMEEG: opensource software for quasistatic bioelectromagnetics. Biomed Eng Online 9 (1), 1–20.

Haueisen, J., Ramon, C., Eiselt, M., Brauer, H., Nowak, H., 1997. Influence of tissue resistivities on neuromagnetic fields and electric potentials studied with a finite element model of the head. IEEE Trans. Biomed. Eng. 44 (8), 727–735.

Hurford, R., Charidimou, A., Fox, Z., Cipolotti, L., Werring, D.J., 2013. Domain-specific trends in cognitive impairment after acute ischaemic stroke. J. Neurol. 260 (1), 237–241.

Kybic, J., Clerc, M., Faugeras, O., Keriven, R., Papadopoulo, T., 2006. Generalized head models for MEG/EEG: boundary element method beyond nested volumes. Physics in Medicine & Biology 51 (5), 1333.

Lalancette, M., Quraan, M., Cheyne, D., 2011. Evaluation of multiple-sphere head models for MEG source localization. Physics in Medicine & Biology 56 (17), 5621.

McCann, H., Pisano, G., Beltrachini, L., 2019. Variation in reported human head tissue electrical conductivity values. Brain Topogr 32 (5), 825–858.

Minjoli, S., Saturnino, G.B., Blicher, J.U., Stagg, C.J., Siebner, H.R., Antunes, A., Thielscher, A., 2017. The impact of large structural brain changes in chronic stroke patients on the electric field caused by transcranial brain stimulation. NeuroImage: Clinical 15, 106–117.

Montes-Restrepo, V., van Mierlo, P., Strobbe, G., Staelens, S., Vandenberghe, S., Hallez, H., 2014. Influence of skull modeling approaches on EEG source localization. Brain Topogr 27 (1), 95–111.

Mosher, J.C., Leahy, R.M., Lewis, P.S., 1999. EEG and MEG: forward solutions for inverse methods. IEEE Trans. Biomed. Eng. 46 (3), 245–259.

Nolte, G., 2003. The magnetic lead field theorem in the quasi-static approximation and its use for magnetoencephalography forward calculation in realistic volume conductors. Physics in Medicine & Biology 48 (22), 3637.

Oostenveld, R., Fries, P., Maris, E., Schoffelen, J.M., 2011. Fieldtrip: open source software for advanced analysis of MEG, EEG, and invasive electrophysiological data. Computational Intelligence and Neuroscience.

Oostenveld, R., Oostendorp, T.F., 2002. Validating the boundary element method for forward and inverse EEG computations in the presence of a hole in the skull. Hum Brain Mapp 17 (3), 179–192.

Piastra, M.C., Cruijsen, J.V.D., Piai, V., Jeukens, F.E., Manoochehri, M., Schouten, A.C., Selles, R.W., Oostendorp, T., 2021a. ASH: an automatic pipeline to generate realistic and individualized chronic stroke volume conduction head models. J Neural Eng 18 (4), 044001.

Piastra, M.C., Nüßing, A., Vorwerk, J., Bornfleth, H., Oostenveld, R., Engwer, C., Wolters, C.H., 2018. The discontinuous Galerkin finite element method for solving the MEG and the combined MEG/EEG forward problem. Front Neurosci 12, 30.

Piastra, M.C., Nüßing, A., Vorwerk, J., Clerc, M., Engwer, C., H. Wolters, C., 2021b. A comprehensive study on electroencephalography and magnetoencephalography sensitivity to cortical and subcortical sources. Hum Brain Mapp 42 (4), 978–992.

Pursiainen, S., Lucka, F., Wolters, C.H., 2012. Complete electrode model in EEG: relationship and differences to the point electrode model. Physics in Medicine & Biology 57 (4), 999.

Pustina, D., Coslett, H.B., Turkeltaub, P.E., Tustison, N., Schwartz, M.F., Avants, B., 2016. Automated segmentation of chronic stroke lesions using linda: Lesion identification with neighborhood data analysis. Hum Brain Mapp 37 (4), 1405–1421.

Sarvas, J., 1987. Basic mathematical and electromagnetic concepts of the biomagnetic inverse problem. Physics in Medicine & Biology 32 (1), 11.

Scherg, M., 1990. Fundamentals of dipole source potential analysis. Auditory evoked magnetic fields and electric potentials. Advances in audiology 6, 40–69.

Schimpf, P.H., Ramon, C., Haueisen, J., 2002. Dipole models for the EEG and MEG. IEEE Trans. Biomed. Eng. 49 (5), 409–418.

Schmidt, C., Wagner, S., Burger, M., van Rienen, U., Wolters, C.H., 2015. Impact of uncertain head tissue conductivity in the optimization of transcranial direct current stimulation for an auditory target. J Neural Eng 12 (4), 046028.

Schrader, S., Westhoff, A., Piastra, M.C., Miinalainen, T., Pursiainen, S., Vorwerk, J., Brinck, H., Wolters, C.H., Engwer, C., 2021. DUNEuro - A software toolbox for forward modeling in bioelectromagnetism. PLoS ONE 16 (6), e0252431.

Stenroos, M., 2016. Integral equations and boundary-element solution for static potential in a general piece-wise homogeneous volume conductor. Physics in Medicine & Biology 61 (22). N606

Stenroos, M., Hauk, O., 2013. Minimum-norm cortical source estimation in layered head models is robust against skull conductivity error. Neuroimage 81, 265–272.

Stenroos, M., Hunold, A., Haueisen, J., 2014. Comparison of three-shell and simplified volume conductor models in magnetoencephalography. Neuroimage 94, 337–348.

Tadel, F., Baillet, S., Mosher, J.C., Pantazis, D., Leahy, R.M., 2011. Brainstorm: a user-friendly application for MEG/EEG analysis. Computational intelligence and neuroscience.

Tona, K.-D., Keuken, M.C., de Rover, M., Lakke, E., Forstmann, B.U., Nieuwenhuis, S., van Osch, M.J., 2017. In vivo visualization of the locus coeruleus in humans: quantifying the test–retest reliability. Brain Structure and Function 222 (9), 4203–4217.

Vorwerk, J., Cho, J.-H., Rampp, S., Hamer, H., Knösche, T.R., Wolters, C.H., 2014. A guideline for head volume conductor modeling in EEG and MEG. Neuroimage 100, 590–607.

Wagner, S., Lucka, F., Vorwerk, J., Herrmann, C.S., Nolte, G., Burger, M., H. Wolters, C., 2016. Using reciprocity for relating the simulation of transcranial current stimulation to the EEG forward problem. Neuroimage 140, 163–173.

Wagner, S., Rampersad, S., Aydin, U., Vorwerk, J., Oostendorp, T., Neuling, T., Herrmann, C., Stegeman, D., Wolters, C., 2013. Investigation of tdcs volume conduction effects in a highly realistic head model. J Neural Eng 11 (1), 016002.

Weinstein, D., Zhukov, L., Johnson, C., 2000. Lead-field bases for electroencephalography source imaging. Ann Biomed Eng 28 (9), 1059–1065.

Wolters, C.H., Anwander, A., Tricoche, X., Weinstein, D., Koch, M.A., S. Macleod, R., 2006. Influence of tissue conductivity anisotropy on EEG/MEG field and return current computation in a realistic head model: a simulation and visualization study using high-resolution finite element modeling. Neuroimage 30 (3), 813–826.

Yan, Y., Nunez, P., Hart, R., 1991. Finite-element model of the human head: scalp potentials due to dipole sources. Med. Biol. Eng. Comput. 29 (5), 475–481.